Low-Phase-Noise Wideband Mode-Switching Quad-Core-Coupled mm-wave VCO Using a Single-Center-Tapped Switched Inductor

Yatao Peng, Jun Yin, *Member, IEEE*, Pui-In Mak, *Senior Member, IEEE*, and Rui P. Martins, *Fellow, IEEE*

***Abstract*— This paper describes a mode-switching quad-core-coupled millimeter-wave (mm-wave) voltage-controlled oscillator (VCO), using a single-center-tapped (SCT) switched inductor for extension of the frequency tuning range (FTR) and improvement of the phase noise (PN). The switches not only serve for in-phase coupling among the VCO cores but also can modify the equivalent tank inductance suitable for coarse frequency tuning. The frequency gaps between the multi-resonant frequencies are controlled by the common-mode (CM) inductance that is precisely set by the lithography fabrication. Together with the tiny varactors for fine frequency tuning, a wide and continuous FTR can be achieved. It is analytically shown that tiny switches (i.e., small parasitic capacitance) for mode selection are adequate to avoid bimodal oscillation, synchronize the VCO cores against resonance frequency mismatches, and prevent PN degradation. A symmetrical layout of SCT switched inductor also aids the VCO to be immune to magnetic pulling. Prototyped in 65-nm CMOS, the VCO exhibits a 16.5% FTR from 42.9 to 50.6 GHz. The PN at 46.03 GHz is −113.1 dBc/Hz at 3-MHz offset, corresponding to a figure-of-merit (FoM) of 183.6 dBc/Hz. The die size is 0.039 mm^2.**

***Index Terms*— Frequency-tuning range (FTR), *LC* tank, millimeter-wave (mm-wave), mode switching, multi-mode resonance, phase noise (PN), switched inductor, voltage-controlled oscillator (VCO).**

I. Introduction

WIRELESS communication standards at millimeter-wave (mm-wave) frequency are trending toward wider channel bandwidth and denser modulation for data rate enhancement. For instance, to cover the 57–65-GHz unlicensed band, a wideband local oscillator (LO) with $>13.3\%$ tuning range is required. On the other hand, the advanced modulation scheme such as 16-quadrature-amplitude modulation (QAM) and beyond demands a stringent LO phase noise (PN) requirement to prevent the error vector magnitude (EVM) degradation [1]. Regrettably, it is a non-trivial task for mm-wave voltage-controlled oscillators (VCOs) to sustain low PN over a wide frequency tuning range (FTR) [2]. Since the quality factor (Q) of the integrated varactor degrades severely at mm-wave frequencies, the compromise between PN and FTR becomes severe if the frequency-tuning element is only the varactor. The typically reported FTR of the 60-GHz VCOs implemented in 65-nm CMOS using a varactor tuning scheme is $<10\%$ [3], [4]. Since the inductor quality factor Q_L increases at an mm-wave frequency, inductive tuning shows the promise to extent FTR [5]–[9]. However, those inductive-tuning methods suffer from a degraded tank Q which limits the maximum figure-of-merit (FoM) to 180 dBc/Hz. To extend the FTR while keeping low PN, the dual-resonant modes of the transformer tank have been explored for coarse frequency tuning [10], [11]. However, due to the imbalanced quality factors of the transformer tank [12] in the two modes, the wideband VCOs using the transformer tank would suffer from a large PN variation between the two modes. Harmonic-extraction or mixing techniques also can aid the FTR, benefitting from the fundamental oscillation at low frequency [13]–[15]. Yet, power-hungry buffers operating at mm-wave frequencies are entailed to boost the output power, due to the limited power of the extracted harmonic components.

To achieve low PN, a small inductor is preferable. For a single-core LC-VCO oscillating at ω_0, the PN at frequency offset $\Delta\omega$ can be expressed as [16]

$$\mathcal{L}(\Delta\omega) = 10 \cdot \log\left[F \cdot \frac{kT}{V_p^2} \cdot \frac{L}{Q_\mathrm{T}} \cdot \frac{\omega_0^3}{(\Delta\omega)^2}\right] \tag{1}$$

where k is Boltzmann's constant, T is the absolute temperature, F is the device excess noise factor, V_p is the differential oscillation amplitude, L is the tank inductance, and Q_T is the tank quality factor. Since the PN is proportional to L/Q_T as long as V_p is kept the same, the achievable PN depends on the minimum value of the L/Q_T ratio. In practice, Q_L and thus Q_T would drop sharply if the inductance is overly small, nullifying the PN reduction due to the use of a small L. To further reduce the PN, multiple VCO cores with an optimal L/Q_T can be coupled in parallel [17]–[19]. Ideally, by coupling N

Manuscript received March 22, 2018; revised July 4, 2018; accepted August 18, 2018. Date of publication September 13, 2018; date of current version October 22, 2018. This paper was approved by Associate Editor Hossein Hashemi. This work was supported in part by Macao Science and Technology Development Fund through SKL Fund and in part by the University of Macau under Grant MYRG-2017-00185. *(Corresponding author: Jun Yin.)*

Y. Peng and J. Yin are with the State Key Laboratory of Analog and Mixed-Signal VLSI, University of Macau, Macau, China (e-mail: junyin@umac.mo).

P.-I. Mak is with the State-Key Laboratory of Analog and Mixed-Signal VLSI and the Faculty of Science and Technology, Department of Electrical and Computer Engineering, University of Macau, Macau, China (e-mail: pimak@umac.mo).

R. P. Martins is with the State-Key Laboratory of Analog and Mixed-Signal VLSI and the Faculty of Science and Technology, Department of Electrical and Computer Engineering, University of Macau, Macau, China, on leave from the Instituto Superior Técnico, University of Lisbon, Lisbon, Portugal.

Color versions of one or more of the figures in this paper are available online at http://ieeexplore.ieee.org.

Digital Object Identifier 10.1109/JSSC.2018.2867269

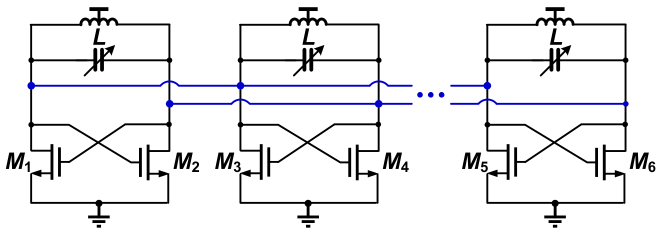

Fig. 1. Multiple VCO cores coupled in parallel allows PN reduction.

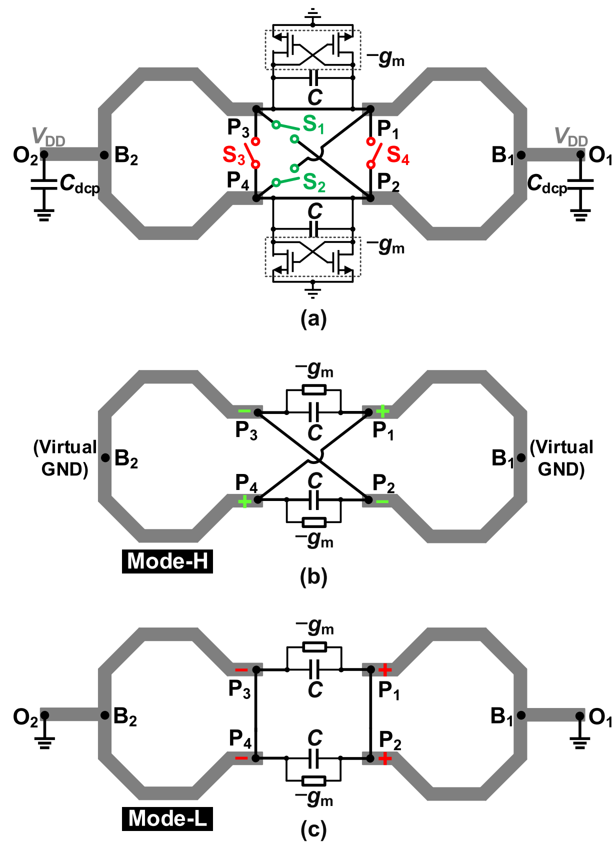

Fig. 2. (a) Proposed switched inductor applied to a dual-core-coupled VCO. (b) Illustration of the tank for Mode-H when the switches S_1 and S_2 are turned on and S_3 and S_4 are turned off. (c) Illustration of the tank for Mode-L when the switches S_3 and S_4 are turned on, and S_1 and S_2 are turned off.

VCO cores in-phase as shown in Fig. 1, the equivalent tank inductance is reduced by N times, with Q_L unchanged. Since the cross-coupled $-g_m$ cells are connected in parallel, the total current goes up by N times for an unchanged V_p. Thus, the PN of an in-phase-coupled N-core VCO is improved by N times.

By coupling multiple VCO cores, the sub-10-GHz wideband mode-switching VCOs [20], [21] enable both PN reduction and FTR extension, by creating multiple oscillation modes. In [20], the coupling capacitor loads the resonator as a fixed capacitor and adds to the parasitic capacitance in one mode which limits the FTR in that mode. In [21], a mode-switching VCO employing a cross-coupled inductor results in a large inductance difference, i.e., around one-quarter of the inductance of a single-loop inductor leading to a large frequency gap between the two oscillation bands. The large frequency gap will result in a discontinuous FTR if directly applied to the mm-wave VCO, where the fine FTR covered by the varactors (typically <10%) becomes much smaller than that of the sub-10-GHz VCOs.

To surmount such a tradeoff between PN and FTR for mm-wave VCOs, this paper proposes a single-center-tapped (SCT) switched inductor that features a flexible control of the inductance ratio between the two oscillation modes. By applying it to the mode-switching quad-core-coupled mm-wave VCO, a small frequency gap between the two frequency bands can be realized without penalizing the tank Q which results in a wider continuous FTR and low PN performance.

After the Introduction, we present the concept of the SCT switched inductor in Section II. In Section III, we apply the proposed SCT switched inductor to design a mode-switching quad-core-coupled VCO with low PN and wide FTR, presenting in detail its mode-switching principle and features to reject the magnetic pulling from other on-chip inductors. Section IV analyzes the design considerations of the switches for mode selection. In Section V, the measurement results of the VCO prototyped in 65-nm CMOS are summarized, and we finally draw the conclusion in Section VI.

II. Proposed Single-Center-Tapped Switched Inductor

First, we illustrate the idea of the switched inductor via a dual-core-coupled VCO [Fig. 2(a)] employing single-turn inductors to obtain a small inductance value at mm-wave frequency. Here, assuming the two inductors on the left and right are identical, the switches S_{1-4} connected between nodes P_{1-4} are ideal with zero turn-on resistance. A pair of large decoupling capacitors C_{dcp} is connected between V_{DD} and ground to realize ac short. When S_1 and S_2 are turned on, while S_3 and S_4 are turned off [Fig. 2(b)], the signals at P_1 and P_2 are differential. Node B_1 (B_2) is the virtual ground, and the inductance of trace O_1B_1 (O_2B_2) is the common-mode (CM) inductance that would not be counted as the total tank inductance. Thus, the VCO will operate at a high frequency in Mode-H. On the other hand, when S_3 and S_4 are turned on, and S_1 and S_2 are turned off [Fig. 2(c)], the signals at P_1 and P_2 are in phase. Thus, the inductance of trace O_1B_1 (O_2B_2) contributes to the overall tank inductance, thereby reducing the oscillation frequency (Mode-L).

Similar to the mode-switching VCO in [20] and [21], assuming no mismatch between the tanks, there is no current flowing through the turn-on switches in the proposed mode-switching VCO using an SCT switched inductor since they are all connected between the nodes that have signals with the same amplitude and phase. Hence, the switches used for coupling the VCO cores as well as selecting the oscillation modes would not degrade the tank Q even when they have non-zero turn-on resistance.

To obtain the explicit expressions for the tank inductance and oscillation frequency in the two oscillation modes, we model the two traces P_1B_1 and P_2B_1 as a transformer and the trace O_1B_1 as a fixed inductor L_{CM}, as shown in Fig. 3(a). Here, L_0 represents the intrinsic inductance of P_1B_1 or P_2B_1

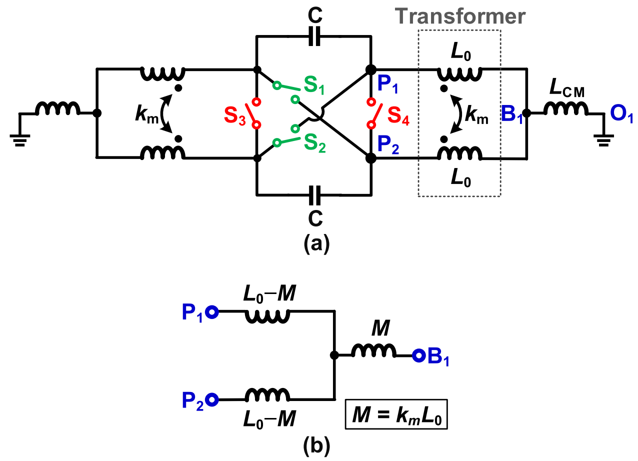

Fig. 3. (a) Tank model of the mode-switching dual-core-coupled VCO. (b) T-model for the transformer.

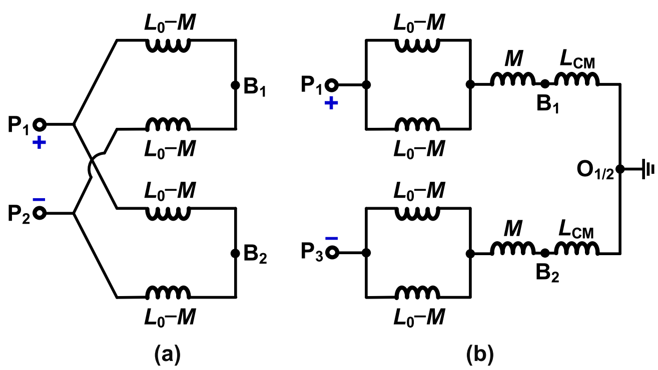

Fig. 4. Equivalent tank inductance of (a) Model-H and (b) Model-L assuming ideal switches.

and k_m models the positive coupling between them.[1] By replacing the transformer with its T-model [Fig. 3(b)], the equivalent tank inductance model for both modes can be obtained as shown in Fig. 4, where the mutual inductance M is defined as $M = k_m L_0$. In Mode-H [Fig. 4(a)], the equivalent tank inductance becomes

$$L_{\mathrm{eq,H}} = L_0 - M = (1 - k_m) L_0 \tag{2}$$

where L_{CM} is excluded since P_1 and P_2 (P_3 and P_4) are excited differentially. $L_{\mathrm{eq,H}}$ is lower than L_0 since the positive magnetic coupling between the P_1B and P_2B cancels part of the differential inductance. Since the equivalent tank capacitance is $2C$, the oscillation frequency of Mode-H can be written as

$$f_{\mathrm{H}} = \frac{1}{2\pi\sqrt{2\,(1-k_m)\,L_0 C}}. \tag{3}$$

In Mode-L [Fig. 4(b)], both the traces $P_1B_1P_2$ ($P_3B_2P_4$) and O_1B_1 (O_2B_2) would contribute to the overall equivalent tank inductance $L_{\mathrm{eq,L}}$ since P_1 and P_2 (P_3 and P_4) are excited in phase. The equivalent inductance from $P_1B_1P_2$ ($P_3B_2P_4$) equals to $L_0 + M$ which is higher than L_0 since the positive magnetic coupling in-turn enhances the equivalent inductance. The existence of trace O_1B_1 (O_2B_2) further increases $L_{\mathrm{eq,L}}$ which is given as

$$L_{\mathrm{eq},L} = L_0 + M + 2L_{\mathrm{CM}} = (1 + k_m)\,L_0 + 2L_{\mathrm{CM}}. \tag{4}$$

Thus, the oscillation frequency of Mode-H will be

$$f_L = \frac{1}{2\pi\sqrt{2\,[(1+k_m)\,L_0 + 2L_{\mathrm{CM}}]\,C}}. \tag{5}$$

The difference between $L_{\mathrm{eq,H}}$ and $L_{\mathrm{eq,L}}$ is caused by the magnetic coupling k_m between traces P_1B_1 (P_3B_2) and P_2B_1 (P_4B_2), as well as the CM inductance from traces O_1B_1 (O_2B_2). Since k_m is weak in a single-turn inductor, $M = k_m L_0$ is usually quite small. According to the electromagnetic (EM) simulation, an octagonal inductor with a radius of 52 μm gives $L_0 \approx 80$ pH and $k_m \approx 0.07$ at 50 GHz, resulting in $M \approx 5.6$ pH. Then, the frequency difference mainly depends on L_{CM} which can be precisely controlled by the length of the metal trace O_1B_1 (O_2B_2).

In the layout, there is no ideal ground plane that can perfectly short the two far away ground nodes in Fig. 2(a). As a result, the parasitic inductance from the ground plane would significantly increase L_{CM}, and make it not well controlled. To overcome this, a novel inductor layout is proposed by flipping both the center taps O_1B_1 and O_2B_2 into the center, so that O_1 and O_2 can be physically merged together as a single node O (Fig. 5). Thus, L_{CM} is well defined by the length of the metal traces OB_1 and OB_2. The positions of ports P_{1-4} are unchanged to facilitate the connection of $-g_{\mathrm{m}}$ cells and switches.

[1]The model of positive coupling is only valid for a single-turn symmetric planar inductor. For a multi-turn symmetric planar inductor, the model should be changed to use a negative coupling between the two equivalent inductors.

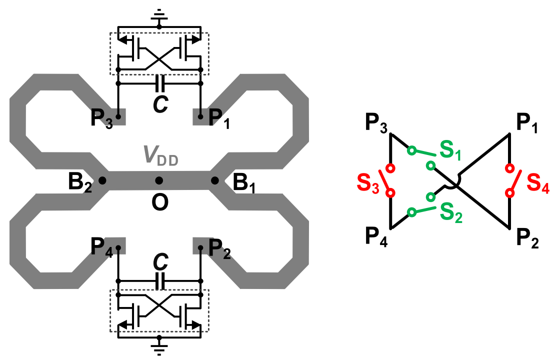

Fig. 5. Dual-core-coupled VCO with an SCT switched inductor.

III. Quad-Core-Coupled VCO Using The Proposed Single-Center-Tapped Switched Inductor

To further reduce the PN, the proposed switched inductor is applied into a quad-core-coupled VCO. Fig. 6 shows the layout floorplan of an SCT switched inductor. The switch ($S_{i,j}$) is employed to connect the corresponding two ports (P_i, P_j). The detailed arrangement of the twelve switches is $S_{1,2}$ (P_1, P_2), $S_{2,3}$ (P_2, P_3), $S_{3,4}$ (P_3, P_4), $S_{4,5}$ (P_4, P_5) $S_{5,6}$ (P_5, P_6), $S_{6,7}$ (P_6, P_7), $S_{7,8}$ (P_7, P_8), $S_{1,8}$ (P_1, P_8), $S_{1,5}$ (P_1, P_5), $S_{2,6}$ (P_2, P_6), $S_{3,7}$ (P_3, P_7), and $S_{4,8}$ (P_4, P_8).

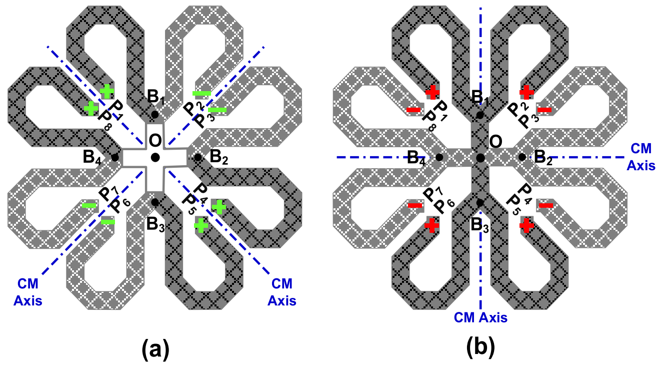

Fig. 6. Port excitations of the quad-core-coupled VCO using the SCT switched inductor in (a) Mode-H and (b) Mode-L.

A. Equivalent Inductance and Qs of Tank Inductor

In Mode-H [Fig. 6(a)], $S_{1,8}$, $S_{2,3}$, $S_{4,5}$, $S_{6,7}$, $S_{1,5}$, $S_{2,6}$, $S_{3,7}$, and $S_{4,8}$, are turned on; $S_{1,2}$, $S_{3,4}$, $S_{5,6}$, and $S_{7,8}$ are turned off. Thus, ports P_1, P_4, P_5, and P_8 (P_2, P_3, P_6, and P_7) are connected together by switches $S_{1,8}$, $S_{4,5}$, $S_{1,5}$, and $S_{4,8}$ ($S_{2,3}$, $S_{6,7}$, $S_{2,6}$, and $S_{3,7}$). Similar to the case for the dual-core-coupled VCO, Nodes B_{1-4} become the virtual ground nodes and the inductances from metal traces OB_1, OB_2, OB_3, and OB_4 will not be counted into the equivalent tank inductance $L_{\text{eq,H}}$. To consider the magnetic coupling effect, we group OP_1P_2 and OP_5P_6 (OP_3P_4 and OP_7P_8) as inductor 1 (inductor 2) together and their equivalent inductance L_A can be directly obtained by using (1) as $L_A = (1-k_1)L_0$ where L_0 is the intrinsic inductance of trace P_1B_1 or P_2B_1 and k_1 is the magnetic coupling coefficient between traces B_1P_1 and B_1P_2. If the magnetic coupling coefficient between inductors 1 and 2 is k_2, the equivalent tank inductance is calculated as

$$L_{\text{eq,H}} = \frac{(1-k_1)(1+k_2)}{2}L_0. \tag{6}$$

Since the adjacent two ports between the inductors 1 and 2 are all excited in phase, the magnetic coupling k_2 enhances the equivalent tank inductance.

In Mode-L [Fig. 6(b)], $S_{1,2}$, $S_{3,4}$, $S_{5,6}$, $S_{7,8}$, $S_{1,5}$, $S_{2,6}$, $S_{3,7}$, and $S_{4,8}$, are turned on; $S_{2,3}$, $S_{4,5}$, $S_{6,7}$, and $S_{1,8}$ are turned off. Thus, ports P_1, P_2, P_5, and P_6 (P_3, P_4, P_7, and P_8) are connected together by switches $S_{1,2}$, $S_{5,6}$, $S_{2,6}$, and $S_{1,5}$ ($S_{3,4}$, $S_{7,8}$, $S_{3,7}$, and $S_{4,8}$). Again we group OP_1P_2 and OP_5P_6 (OP_3P_4 and OP_7P_8) as inductor 1 (inductor 2) and their equivalent inductance can be given as $L_B = (1+k_1)L_0/4 + L_{\text{CM}}/2$. Now, the adjacent two ports between inductors 1 and 2 are all excited differentially. The equivalent tank inductance becomes

$$L_{\text{eq,L}} = \frac{(1+k_1)(1-k_2)}{2}L_0 + (1-k_2)L_{\text{CM}}. \tag{7}$$

In the SCT inductor layout as shown in Fig. 5, k_1 is larger than k_m in the conventional inductor layout as shown in Fig. 2(a) since the traces B_1P_1 and B_1P_2 are much closer. Interestingly, the magnetic coupling k_2 helps nullifying the effect of k_1 on both $L_{\text{eq,H}}$ and $L_{\text{eq,L}}$ according to (5) and (6). The EM simulation reveals that k_1 and k_2 in the SCT switched inductor (Fig. 6) with a radius of 55 μm are 0.13 and 0.15, respectively, resulting in $(1-k_1)(1+k_2) \approx 1$ and $(1+k_1)(1-k_2) \approx 0.96$. Thus, the difference between $L_{\text{eq,L}}$ and $L_{\text{eq,H}}$ becomes $0.85L_{\text{CM}} - 0.02L_0$, which mainly depends on L_{CM} and can be well controlled to achieve small frequency gap between the two modes.

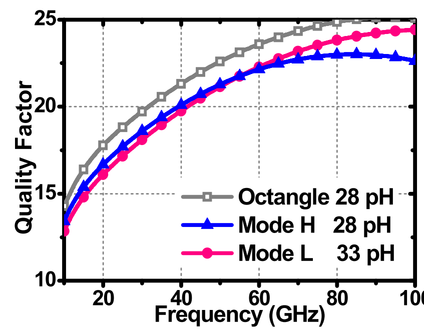

Fig. 7. EM simulated Qs of the SCT switched inductor and the conventional single-turn octangle inductor.

Since the parasitic capacitance of the switch changes between ON and OFF states, it may also affect the oscillation frequencies in the Mode-H and Mode-L. The switch arrangement in this design guarantees that there are always two switches in ON state and one switch in OFF state connected to one output node in both Mode-H and Mode-L so that their parasitic capacitance would have a negligible effect on the oscillation frequency.

Qs of the proposed SCT switched inductor in both Mode-H and Mode-L are compared with that of a classic octagonal inductor with a similar inductance using EM simulation, where the modes are set by ideal switches. As plotted in Fig. 7, Qs of the proposed inductor only degrades by 7% from 22.6 to 21 at 50 GHz. If we assume a varactor Q of $\sim$10, tank Q degradation would be negligibly reduced from 6.93 to 6.77 (2.3%). Also, the inductor Qs in both Mode-H and Mode-L are almost identical when the frequency is <60 GHz.

B. Magnetic Pulling Rejection

The typical *LC*-VCO is sensitive to magnetic pulling from other circuits with on-chip inductors, e.g., the PA, if the VCO is operating at the harmonically related frequencies of these circuits. An effective way to reduce this magnetic pulling is to employ an eight-shaped inductor in the VCO [22], [23]. The proposed inductors can also reject the magnetic pulling naturally due to its symmetrical layout. Ideally, the magnetic pulling from the direction of the CM axes as shown in Fig. 6 will be fully cancelled.

To show the magnetic pulling rejection, here we use an octagonal inductor to emulate the attacker and another octagonal inductor to emulate the victim as a reference [Fig. 8(a)]. Then, we replace the victim with our SCT switched inductor and put the attacker on two different directions, i.e., Dir1 and Dir2, as shown in Fig. 8(b). The strength of injection pulling is determined by the EM simulation of power gain from the attacker (Port 1) to the victim (Port 2), i.e., S_{21}. Table I summarizes the simulation results of the magnetic pulling rejection improvement when compared with the reference at 50 GHz. As expected, when the attacker is put at either the CM axis of the Mode-H (Dir2) or Mode-L (Dir1), a significant improvement of 57.8 or 62.2 dB is achieved. Even when the

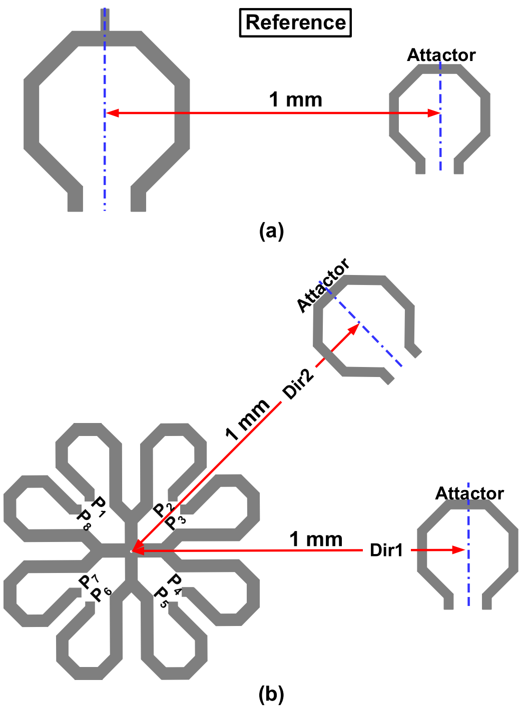

Fig. 8. Floor plan of the EM simulation for injection pulling from other circuits with on-chip inductors. (a) Victim is a conventional octangle inductor as a reference. (b) Victim is the SCT switched inductor.

TABLE I
EM SIMULATED MAGNETIC PULLING IMPROVEMENT

	Dir1 (dB)	Dir2 (dB)
Mode-H	−24.9	−57.8
Mode-L	−62.2	−20.5

attacker is not put on the CM-axis, e.g., on Dir1 for Mode-H or Dir2 for Mode-L, still a 24.9-or 20.5-dB improvement can be obtained.

C. Circuit Implementation

Fig. 9(a) shows the schematic of the mode-switching quad-core-coupled VCO using the proposed SCT switched inductor. There are four cross-coupled $-g_m$ cells and the tank capacitor C_T connected between the two ports that are always excited differentially in both Mode-H and Mode-L (Fig. 6), to compensate the tank loss. The dual modes created by SCT switched inductor are used for coarse frequency tuning, while the fine frequency tuning within each mode is obtained by 4-bit binary-switched varactors. A small A-MOS varactor is employed for continuous frequency tuning.

Using the $L_{\text{eq,H}}$ and $L_{\text{eq,L}}$ expressions from (5) and (6), the oscillation frequencies in each mode can be estimated as

$$f_H = \frac{1}{2\pi\sqrt{(1-k_1)(1+k_2)L_0 C_T}} \tag{8}$$

$$f_L = \frac{1}{2\pi\sqrt{[(1+k_1)(1-k_2)L_0 + 2(1-k_2)L_{CM}]C_T}}. \tag{9}$$

If we choose $L_0 = 85$ pH, $L_{CM} = 17$ pH, $k_1 = 0.13$, and $k_2 = 0.15$, the frequency ratio can be calculated as $f_H/f_L = 1.16$. We use the EM simulated scatter parameters

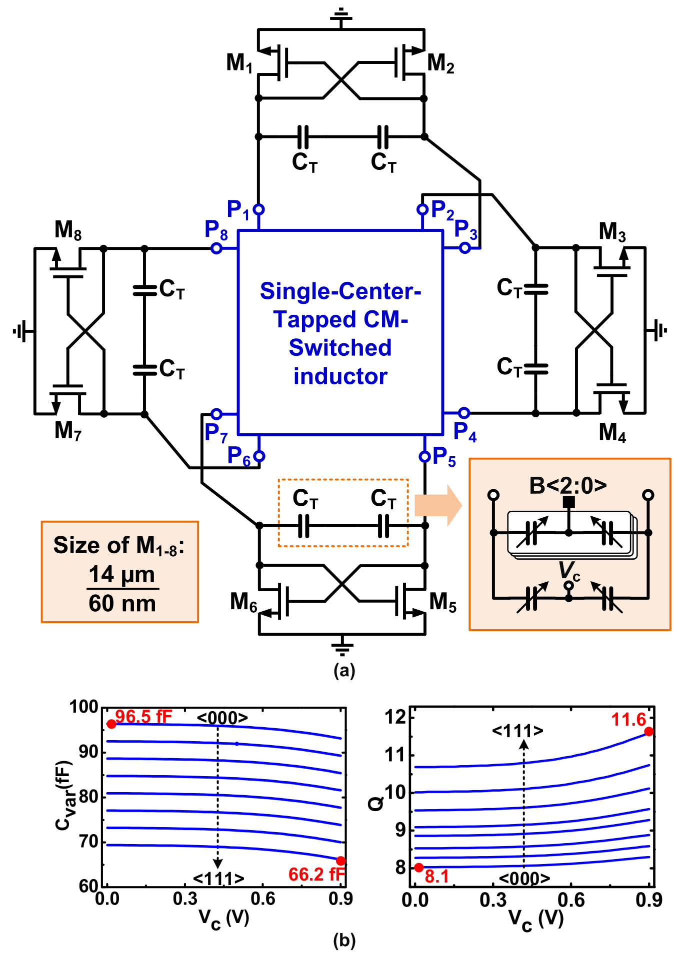

Fig. 9. (a) Schematic of the quad-core-coupled VCO using the proposed SCT switched inductor. (b) Simulated capacitance and Q of the varactor bank.

of the proposed inductor to construct a resonant LC tank. Two resonant frequencies, i.e., f_H and f_L, can be observed as predicted, and their ratio is 1.15 which is quite close to the calculation results.

The A-MOS varactors all use a minimum figure length (200 nm) to maintain a high Q. As shown in Fig. 9(b), the simulated minimum ($C_{v,\min}$) and maximum ($C_{v,\max}$) capacitance of the varactor bank are 66.2 and 96.5 fF, respectively, corresponding to a $C_{v,\max}/C_{v,\min}$ ratio of 1.46. Qs of varactor bank at $C_{v,\min}$ and $C_{v,\max}$ are 8.1 and 11.6, respectively. The FTR of one frequency band can be expressed as

$$\text{FTR} = 2 \cdot \frac{\sqrt{A_1 + A_2} - \sqrt{1 + A_2}}{\sqrt{A_1 + A_2} + \sqrt{1 + A_2}} \tag{10}$$

where $A_1 = C_{v,\max}/C_{v,\min}$, $A_2 = C_p/C_{v,\min}$, and C_p is the tank parasitic capacitance. By putting $C_{v,\max} = 96.5$ fF, $C_{v,\min} = 66.2$ fF, and $C_p = 45.6$ fF into (10), the estimated FTR of one frequency band of our mode-switching VCO is $\sim$12%. By combining the two frequency bands together with sufficient overlap, the proposed VCO can achieve a total FTR of 17%. Compared with a conventional quad-core-coupled VCO that employs four 85-pH classical octagonal inductors, the proposed mode-switching VCO would have little area penalty since the core area is dominated by the inductors. The C_p of the conventional quad-core-coupled VCO is reduced to 41.6 fF by removing the four switches in OFF state. To keep maximum frequency unchanged, the $C_{v,\min}$ is increased to 70.2 fF. According to (10), a larger $C_{v,\max}/C_{v,\min}$ ratio of 1.65 is needed for the conventional quad-core-coupled VCO to attain over a 17% FTR, which degrades the worst case Q of the varactor bank to 5.5. Assuming an inductor Q of ~21, the worst case tank Qs of the mode-switching and conventional VCOs are 5.9 and 4.4, respectively. Hence, the output amplitude V_p of the conventional VCO is reduced by 1.34× compared with that of the mode-switching VCO if the power consumption is unchanged. According to (1), the reduced tank Q and output amplitude of the conventional VCO result in a PN degradation of ~3.8 dB compared with this paper. Thus, the proposed method reveals a solution to attain low PN and a wide FTR at mm-wave frequency in a VCO design.

The VCO prototype targets the support to a dual-conversion receiver that employs two LO frequencies with the relationship of $f_{\mathrm{LO2}} = f_{\mathrm{LO1}}/4$ [5]. To cover the 57–65 GHz unlicensed band, the VCO (LO1) is designed to cover the FTR from 45.6 to 52 GHz.

IV. Design of the Switches For Mode Selection

A. Avoiding the Bimodal Oscillation

Assuming that the mode-switchable inductor is symmetric and the four $-g_{\mathrm{m}}$ cells and tank capacitors C_{T} are identical, the amplitude of tank impedance looked from ports $\mathrm{P_1P_3}$ [Fig. 9(a)] will have two peaks located at f_{L} and f_{H} without the switches for mode selection.[2] Since the phase of the tank impedance is equal to zero at both f_{L} and f_{H}, the VCO can potentially oscillate at either f_{L} or f_{H}, or concurrently oscillate at both frequencies if g_{m} provided by M_{1-8} is large enough [24]. This stability issue can be solved by adding the switches for mode selection. As illustrated in Fig. 10, the magnitude of the tank impedance at undesired resonant frequency can be reduced by decreasing the turn-on resistance R_{ON} of the switch. Also, the phase of the tank impedance at the undesired resonant frequency will stop crossing zero if R_{ON} is small enough. On the other hand, the impedance and Q of the tank at the desired resonant frequencies are unaffected by R_{ON}. According to the simulations (Fig. 10), the bimodal oscillation can be completely eliminated by choosing $R_{\mathrm{ON}} < 1$ kΩ.

B. Frequency Synchronization

The mismatch between the LC-tanks of four VCO cores may cause their free-running frequencies to deviate from each other. If R_{ON} is oversized, the free-running frequencies of the four cores may fail to synchronize which would produce injection pulling spurs at the output [18]. Thus, R_{ON} must be small to guarantee the frequency synchronization in the presence of mismatch.

To study the influence of R_{ON} on the frequency synchronization, we can treat the multi-core VCOs as an injection-locked

[2]Due to the symmetrical property of the single-center-taped inductor, the tank impedance looked from ports $\mathrm{P_1P_3}$ or $\mathrm{P_2P_4}$ or $\mathrm{P_5P_7}$ or $\mathrm{P_6P_8}$ will be the same.

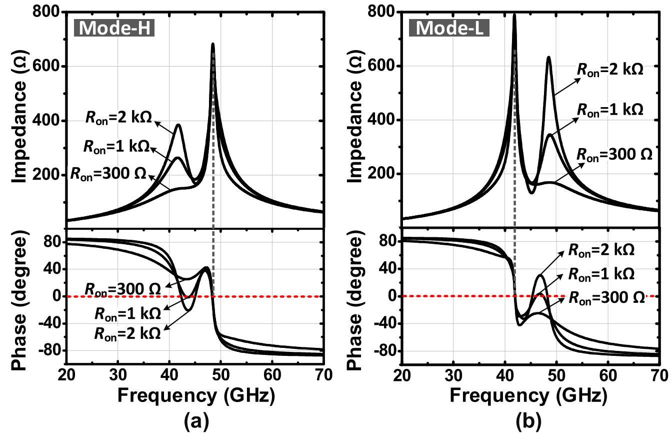

Fig. 10. Simulated amplitude and phase response of the tank impedance for (a) Mode-H and (b) Mode-L. ($L_0 = 85$ pH, $L_{\mathrm{CM}} = 17$ pH, $k_2 = 0.15$, and $Q_{\mathrm{T}} = 15$).

system, and determine the maximum R_{ON} that can still ensure the proper locking in the presence of certain free-running frequency deviations. For example, for a dual-core-coupled VCO with mismatches between the resonant frequencies of each core, we can consider one VCO as an aggressor which injects a current I_{inj} at frequency ω_1 into another VCO (victim) resonating at ω_2, as shown in Fig. 11(a). Here, we only use half circuit of each tank for analysis and assume $L_1 = L_{\mathrm{T}} + \Delta L_1$ ($L_2 = L_{\mathrm{T}} + \Delta L_2$) and $C_1 = C_{\mathrm{T}} + \Delta C_1$ ($C_2 = C_{\mathrm{T}} + \Delta C_2$) where L_{T} and C_{T} represent the nominal tank inductance and capacitance while ΔL_1 (ΔL_2) and ΔC_1 (ΔC_2) are induced by the mismatch which should be much smaller than L_{T} and C_{T}, respectively. Then, the parallel impedances and quality factors of both tanks are approximately R_p and Q_{T}. According to [18] and [25], the locking range ω_{L} and pulling strength η can be given as

$$\omega_{\mathrm{L}} \approx \frac{\omega_2}{2Q_{\mathrm{T}}} \cdot \frac{I_{\mathrm{inj}}}{I_{\mathrm{osc}}} \tag{11}$$

$$\eta \approx \frac{\omega_{\mathrm{L}}}{|\omega_2 - \omega_1|}. \tag{12}$$

Assuming that the two VCOs will be locked to the frequency $\omega_F = (\omega_1 + \omega_2)/2$, the injection current I_{inj} magnitude is

$$|I_{\mathrm{inj}}| = \frac{|V_{\mathrm{osc}}|}{|R_{\mathrm{ON}} + Z_{\mathrm{tank1}}(\Delta\omega_n)|} \tag{13}$$

$$Z_{\mathrm{tank1}}(\Delta\omega_n) \approx \frac{jR_p\Delta\omega_n}{\omega_2 Q_{\mathrm{T}} + j\Delta\omega_n} \tag{14}$$

where $\Delta\omega_n = (\omega_2 - \omega_1)/2$. To maintain the lock condition, η should be larger than 1. Assuming $\omega_2^2 \gg \Delta\omega_n^2$, the maximum R_{ON} that can still guarantee it is

$$R_{\mathrm{ON,max}} = \frac{R_p}{2Q_{\mathrm{T}}}\frac{\omega_2}{\Delta\omega_n} \approx \frac{L_{\mathrm{T}}}{2}\frac{\omega_F^2}{\Delta\omega_n}. \tag{15}$$

Given the ω_2 and $\Delta\omega_n$, the $R_{\mathrm{ON,max}}$ will only depend on the tank inductance L_{T}. If we replace $\Delta\omega_n$ with $(\omega_2 - \omega_1)/2$, the derived (15) is consistent with (8) in [19] obtained through phase and amplitude mismatch analysis.

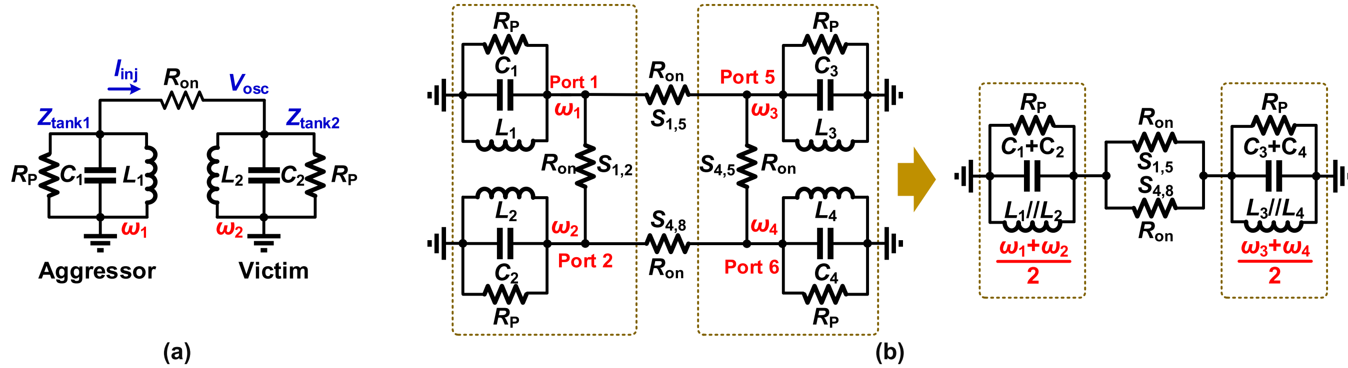

Fig. 11. Equivalent circuits for the frequency synchronization analysis of (a) dual-core coupled VCO and (b) mode-switching quad-core-coupled VCO in Mode-H.

The analysis for dual-core-coupled VCO can be extended to the proposed mode-switching quad-core coupled VCO. Fig. 11(b) shows the equivalent half circuit tanks in Mode-H. Assuming resonant frequencies of the four cores are ω_1, ω_2, ω_3, and ω_4, respectively, the maximum frequency difference can be defined as $\Delta\omega_{\max} = \max\{\omega_1, \omega_2, \omega_3, \omega_4\} - \min\{\omega_1, \omega_2, \omega_3, \omega_4\}$. The final frequency after synchronization will be $\omega_F = (\omega_1 + \omega_2 + \omega_3 + \omega_4)/4$.

The strategy is to synchronize VCO cores 1 and 2 (3 and 4) separately at first. Assuming cores 1 and 2 (3 and 4) are synchronized through only one switch $S_{1,2}$ ($S_{4,5}$) and the tank nominal inductance for each core is L_T, $R_{ON,\max}$ can be given by (15) with $\Delta\omega_n$ replaced by $\max\{|\omega_2 - \omega_1|, |\omega_4 - \omega_3|\}/2$.

After the first-step synchronization, the VCO cores 1 and 2 (3 and 4) are merged into a new VCO called core A (core B). The VCO cores A and B have new resonant frequencies of $(\omega_1 + \omega_2)/2$ and $(\omega_3 + \omega_4)/2$, respectively, given that the oscillating currents of different cores are approximately equal. Their nominal tank inductance is $L_T/2$, which is reduced by half compared with VCO cores 1–4. The second step is to synchronize the VCO cores A and B which are connected by two switches ($S_{1,5}$ and $S_{4,8}$) in parallel, as shown in Fig. 11(b). The $R_{ON,\max}$ can also be obtained by (15) with $\Delta\omega_n$ replaced by $|(\omega_3 - \omega_1) + (\omega_4 - \omega_2)|/4$.

To ensure a successful synchronization in both the first and second steps, the switch turn-on resistance must be smaller than $R_{ON,\max}$ in both steps. For the worst case situation when $\omega_1 = \omega_2 < \omega_3 = \omega_4$, the $R_{ON,\max}$ can be obtained by (15) with $\Delta\omega_n$ replaced by $\Delta\omega_{\max}$. As shown in Fig. 12, $R_{ON,\max}$ obtained from equation agrees well with the simulation results under a different L_T. According to the Monte-Carlo simulation, the standard deviation σ of the resonant frequency of one VCO core with $L_T = 80$ pH is ~25 MHz. Then, $\Delta\omega_{\max}$ can be estimated by $6\sigma \approx 150$ MHz, which requires an $R_{ON,\max}$ of ~7 kΩ.

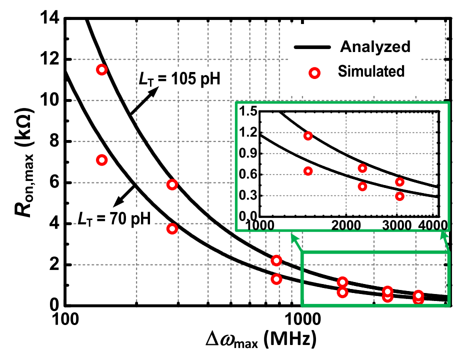

Fig. 12. Simulated and calculated $R_{ON,\max}$ versus $\Delta\omega_{\max}$ for Mode-H under the worst case frequency arrangement ($f_F = 47.6$ GHz).

C. Phase Noise

The interconnected resistors influence PN through two mechanisms, one is the randomness of the oscillation between the VCO cores [18], another is the mismatches of the oscillating frequency [19]. Even without the resonant frequency mismatch between the VCO cores, R_{ON} of the switches would affect the PN performance of the coupled VCO since the presence of PN would cause the oscillation frequency of each VCO core to deviate from f_0 ($f_0 = f_H$ or f_L) randomly, which will induce non-zero ac current flowing through the switches and thereby degrades the PN. The relationship between the PN and R_{ON} for the quad-core-coupled VCO can be deduced using time invariant model as [18]

$$\mathcal{L}(\Delta\omega) = 10\log\left(F\frac{4kTR_p}{V_p}\frac{|Z_{eq}|^2}{R_p^2}\right) \tag{16}$$

$$|Z_{eq}|^2 = \frac{1}{16}\cdot|Z_{tank}(\Delta\omega)|^2\cdot\frac{16R_{ON}^2 + |Z_{tank}(\Delta\omega)|^2}{4R_{ON}^2 + |Z_{tank}(\Delta\omega)|^2} \tag{17}$$

$$|Z_{tank}(\Delta\omega)| = \left|\frac{1}{2}\frac{R_p\omega_0}{Q\Delta\omega}\right|. \tag{18}$$

Fig. 13(a) shows the influence of R_{ON} on PN enhancement at different $\Delta f = \Delta\omega/2\pi$ of the quad-core-coupled VCO based on (16)–(18) and simulation. The PN enhancement becomes less effective as Δf and R_{ON} increases. By choosing a R_{ON} of 260 Ω, the degradation of PN enhancement is only ~0.1 dB even at a 20-MHz offset frequency.

On the other hand, the interconnected resistors degrade PN further when component mismatches are taken into consideration. As two VCO cores with different frequencies couple to each other, the locked and steady oscillating frequency ω_F deviates from the intrinsic tank resonant frequency $\omega_{1,2}$

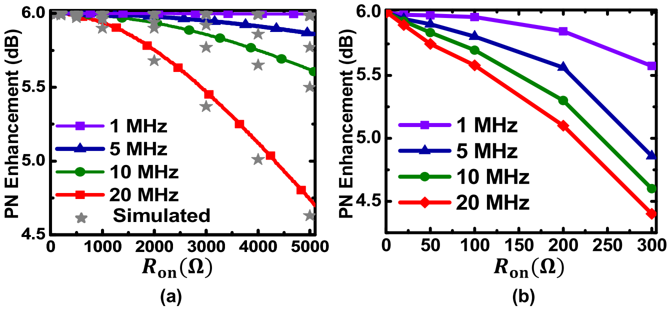

Fig. 13. PN enhancement versus R_{ON} at different offset frequencies for Mode-H at $L_0 = 85$ pH, $C_T = 80$ fF, and $Q_T = 15$: (a) without frequency mismatch ($\omega_1 = \omega_2 = \omega_3 = \omega_4$) and (b) with 7% frequency mismatch ($\omega_1 = \omega_2 < \omega_3 = \omega_4$).

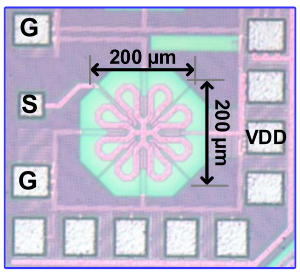

Fig. 14. Chip micrograph.

($\omega_F \neq \omega_{1,2}$). Thus, the oscillation amplitude reduces since effective tank impedance magnitude also deviates from the highest point, which worsens PN based on (15). $\omega_F \neq \omega_{1,2}$ also leads to phase shift for the oscillation signals, which adds PN penalty. PN degradation is in proportion to the maximum frequency mismatch of among VCO cores ($\Delta\omega_{\max}$), and greater mismatch needs smaller R_{ON} to avoid large PN penalty. For our adopted ring coupling interconnection network as shown in Fig. 11(b), the worst case of PN degradation is happened when $\omega_1 = \omega_2 < \omega_3 = \omega_4$ for a given $\Delta\omega_{\max}$ [19], which is the same as the above-mentioned analyzed results of worst case for frequency synchronization. Fig. 13(b) illustrates the simulated PN enhancement against R_{ON} for 7% frequency mismatch of the four coupled VCO under worst case. It can be seen that PN is deteriorated more apparently due to mismatch, and for the choice of R_{ON} of 260 Ω, it introduce about 1.5-dB PN penalty at a 20-MHz offset frequency.

V. Measurement Results

The mode-switching quad-core-coupled VCO is prototyped in 65-nm low power (LP) CMOS process occupying a die area of 0.039 mm^2 (Fig. 14). We realize the switches for mode selection with thin-oxide PMOS transistors with $W/L = 7\ \mu$m/60 nm and $R_{ON} \approx 260\Omega$, which is adequately small to avoid the bimodal oscillation, ensure the synchronization between the four cores, and achieve 4.5-dB PN enhancement at 20 MHz when compared with the single-core VCO even accounted 7% frequency mismatch. When turned off, the gate of the switch is biased at 0.9 V, which can guarantee that the resistance of the turn-off switch is much higher than that of the turn-onswitch for most of the

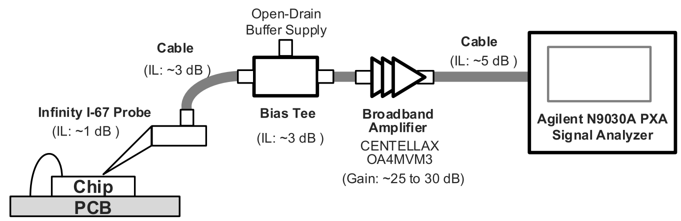

Fig. 15. PN measurement setup.

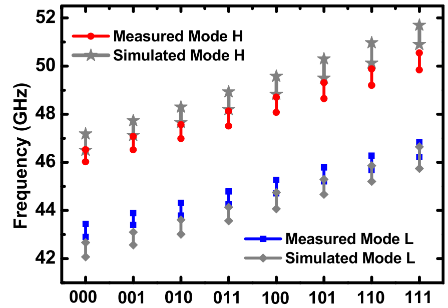

Fig. 16. Measured and simulated frequency-tuning curves.

time within one cycle at an output swing between 0.4 and 1.36 V. The open-drain buffer is employed to extract the oscillating signal from P_1 for testing purposes, while other seven ports are also installed with the same buffer to balance the loading impedance. Fig. 15 shows the PN measurement setup. We employ a broadband amplifier to compensate the large insertion loss (IL) from the cables, the probe, and the Bias Tee which help to maintain a large signal power at the input of the signal analyzer.

The VCO prototype consumes ~21 mA at 0.9 V. Fig. 16 shows the comparison of the simulated and measured frequency tuning curves. The measured FTRs are from 42.9 to 46.8 GHz in Mode-L and from 46.03 to 50.6 GHz in Mode-H. The discrepancy between the measurements and the simulation results is likely caused by the inaccuracy of the EM simulation and the device model which overestimates the value of L_{CM} and underestimates the parasitic capacitance. Fig. 17 displays the measured PN curves at the two typical frequencies of Modes-H and Mode-L, obtained by averaging five measurements. The measured PNs at 43.43 and 46.03 GHz are −112.5 and −113.1 dBc/Hz at a 3-MHz offset frequency, respectively. The estimated $1/f^3$ PN corner frequency is ~680 and ~710 kHz at 43.43 and 46.03 GHz, respectively. Fig. 18 shows the measured PNs and FoMs at 3-MHz offset frequency across the entire frequency range. The measured PN lies between −111.2 and −115.6 dBc/Hz, corresponding to an FoM between 181.1 and 186.6 dBc/Hz.

The maximum output voltage of the designed mode-switching VCO is ~1.36 V at $V_{DD} = 0.9$ V, which is slightly higher than the standard supply voltage of 1.2 V. To evaluate the long-term reliability due to the time-dependent dielectric breakdown which is the main failure mechanism for the VCO, the oxide breakdown scaled model and measured data given in [26] and [27] can be utilized. The lifetime for the eight thin-oxide $-g_m$ transistors with a gate oxide

TABLE II
PERFORMANCE SUMMARY AND COMPARISON

	Topology	Frequency (GHz)	V_{DD} (V)	Power (mW)	PN @ 1MHz (dBc/Hz)	FoM(8) @ 1MHz (dBc/Hz)	FoM_T(9) (dBc/Hz)	Core Area (mm^2)	Technology
This work	Single-Center-Tapped Switched Inductor	42.9~50.6 (16.5%)	0.9	20.9 ~ 21.5	−101.6 ~ −106.1(3)	181.1 ~ 186.6(3)	185.3~190.8	0.039	65 nm CMOS
JSSC'11 [5]	D-Controlled-Artificial-Dielectric	42.1~53 (22.9%)	1.0	16	−97.5	179.5	186.7	0.008	32 nm CMOS
JSSC'13 [7]	Magnetically Tuned Transformer	57.5~76.2 78.5 ~ 90.1 (41.4%)	1.2	8.4 ~ 10.8	−84.6 ~ −92.2 (4)	172 ~ 180	184.2~192.2	0.03	65 nm CMOS
JSSC'15 [13]	2nd Harmonic Extraction	46.4~58.1 (22.4%)	1.0	54 (2)	−89	173 (2)(5)	180	0.137 (7)	32 nm SOI
JSSC'16 [14]	3rd Harmonic Extraction	48.4~62.5 (25.4%)	0.7/ 1.0	24 (2)	−98.7 ~ −100.1	179 ~ 181.9 (2)	187~189.9	0.089 (7)	40 nm CMOS
JSSC'16 [15]	Fundamental and 2nd harmonic self-mixing	52.8 ~ 62.5 (16.8%)	1.2	7.6	−98.3 ~ −100.6	184.7 ~ 186.3	189.2~190.8	0.2	0.13 μm CMOS
JSSC'17 [19]	Switch-Coupled VCO + Frequency Quadrupler	68.8~80.3 (15%)	1.2	50	−106 ~ −108.1	187.2 ~ 188.3	189.5~191.8	0.6	55 nm BiCMOS
JSSC'17 [9]	Switched Coupled Inductor DCO	50.2 ~ 66.5 (28%)	1.0	9.0	−90.8 ~ −96	176.7 ~ 179.3	185.6~188.2	0.03 (7)	65 nm CMOS
ISSCC'13 [6]	Inductor Splitting	33.6 ~ 46.2 (31.6%)	1.2	21.5	−95.2 ~ −98 (4)	177.5 ~ 180	187.5~189.9	0.0084	32 nm CMOS
TCAS-I'14 [8]	Switching Inductor Loaded Transformer	57 ~ 65.5 (14.2%)	1.0	6.0	−85.9 ~ −90.8 (4)	176.2	179.2	0.03	65 nm CMOS
TCAS-I'15 [10]	Switchable-Coupled VCO	55.7~66 (1) (17.2%)	1.2	11.2 ~ 19.1	−87.5 ~ −93.5	176.2 (6)	180.9	0.045 (7)	0.18 μm BiCMOS
TCAS-I'16 [11]	Switched-transformer VCO	62.1~69.5 70.1~78.3 (22.3%)	N/A	7.7 ~ 8.8	−84.5 ~ −90.9	171.5 ~ 179.3	178.5~186.3	0.012	65 nm CMOS

(1) Single-ended output (2) Includes the buffer power consumption (3) Normalized from 3MHz offset in the original measured data
(4) Normalized from 10MHz offset in the original measured data (5) For the worst case (6) For the best case (7) Estimated from the chip photo
(8) $\mathrm{FoM} = -\mathrm{PN} + 20\log(\omega_0/\Delta\omega) - 10\log(P_{\mathrm{diss}}/1\ \mathrm{mW})$ (9) $\mathrm{FoM_T} = \mathrm{FoM} + 20\log(\mathrm{FTR}[\%]/10)$

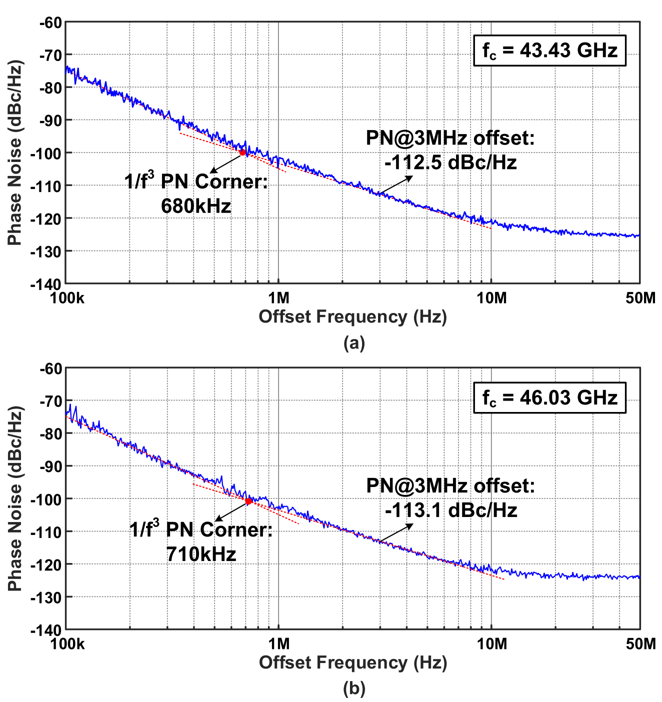

Fig. 17. Measured PN versus offset frequencies at carrier frequencies of (a) 43.43 GHz (Mode-L) and (b) 46.03 GHz (Mode-H).

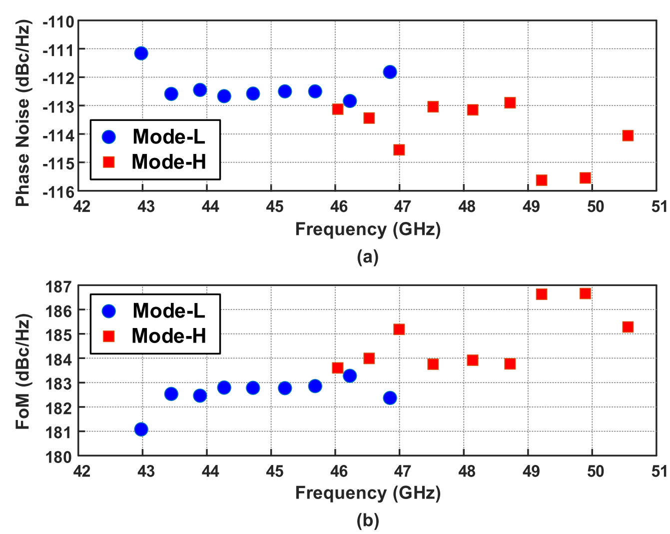

Fig. 18. Measured (a) PN and (b) FoM at 3-MHz offset versus carrier frequencies.

area of 8.4 μm^2 can be calculated and it is $\sim 2.6 \times 10^{12}$ s (> a 10-year standard) for 0.01% failure rate at 140 °C.

Table II summarizes the measurement results and shows the comparison of the work with recent arts. Our quad-core-coupled VCO using the proposed SCT switched inductor can achieve a better FoM compared with other VCOs with inductive tuning schemes [5]–[9], the transformer-based dual-mode VCOs [10], [11], and the VCO using the harmonic-extraction technique [13], [14]. Although the VCO with the fundamental and second harmonic self-mixing [15] shows a higher FoM, extra power-hungry buffers are entailed to recover a similar output swing as our VCO directly operating at the fundamental frequency. The switch-coupled VCO together with a frequency quadrupler [19] can achieve excellent PN and FoM performances. Yet, its area is 15× larger than our design, since it couples four fundamental VCOs operating at a lower frequency of 20 GHz.

VI. Conclusion

An SCT switched inductor has been proposed to achieve in-phase coupling among multiple VCO cores, and create multi-resonant modes by changing the equivalent tank inductance. It can be used in a multi-core-coupled VCO to achieve wide FTR and low PN, simultaneously, at mm-wave frequencies. The inductor is immune to magnetic pulling from the direction of the CM axes. The design of switches for mode-selection shows that a small transistor size is adequate to is as follows:

1) avoid the bimodal oscillation;
2) synchronize multiple VCO cores in the presence of resonance frequency mismatches;
3) prevent the PN degradation.

A 42.7–51-GHz mode-switching quad-core VCO has been prototyped in 65 nm CMOS. It measures a PN at 3-MHz offset frequency between −111.2 and −115.6 dBc/Hz, corresponding to an FoM of 181.1–186.6 dBc/Hz.

References

[1] K. Okada *et al.*, "A 60-GHz 16QAM/8PSK/QPSK/BPSK direct-conversion transceiver for IEEE802.15.3c," *IEEE J. Solid-State Circuits*, vol. 46, no. 12, pp. 2988–3004, Dec. 2011.

[2] S. Elabd, S. Balasubramanian, Q. Wu, T. Quach, A. Mattamana, and W. Khalil, "Analytical and experimental study of wide tuning range mm-Wave CMOS LC-VCOs," *IEEE Trans. Circuits Syst. I, Reg. Papers*, vol. 61, no. 5, pp. 1343–1354, May 2014.

[3] D. D. Kim *et al.*, "A 70 GHz manufacturable complementary LC-VCO with 6.14 GHz tuning range in 65 nm SOI CMOS," in *IEEE Int. Solid-State Circuits Conf. (ISSCC) Dig. Tech. Papers*, Feb. 2007, pp. 540–541.

[4] U. Decanis, A. Ghilioni, E. Monaco, A. Mazzanti, and F. Svelto, "A low-noise quadrature VCO based on magnetically coupled resonators and a wideband frequency divider at millimeter waves," *IEEE J. Solid-State Circuits*, vol. 46, no. 12, pp. 2943–2954, Dec. 2011.

[5] D. Murphy *et al.*, "A low phase noise, wideband and compact CMOS PLL for use in a heterodyne 802.15.3c transceiver," *IEEE J. Solid-State Circuits*, vol. 46, no. 7, pp. 1606–1617, Jul. 2011.

[6] E. Mammei, E. Monaco, A. Mazzanti, and F. Svelto, "A 33.6-to-46.2 GHz 32 nm CMOS VCO with 177.5 dBc/Hz minimum noise FOM using inductor splitting for tuning extension," in *IEEE Int. Solid-State Circuits Conf. (ISSCC) Dig. Tech. Papers*, Feb. 2013, pp. 350–351.

[7] J. Yin and H. C. Luong, "A 57.5-90.1-GHz magnetically tuned multimode CMOS VCO," *IEEE J. Solid-State Circuits*, vol. 48, no. 8, pp. 1851–1861, Aug. 2013.

[8] W. Fei, H. Yu, H. Fu, J. Ren, and K. S. Yeo, "Design and analysis of wide frequency-tuning-range CMOS 60 GHz VCO by switching inductor loaded transformer," *IEEE Trans. Circuits Syst. I, Reg. Papers*, vol. 61, no. 3, pp. 699–711, Mar. 2014.

[9] A. I. Hussein, S. Vasadi, and J. Paramesh, "A 50–66-GHz phase-domain digital frequency synthesizer with low phase noise and low fractional spurs," *IEEE J. Solid-State Circuits*, vol. 52, no. 12, pp. 3329–3347, Dec. 2017.

[10] Q. Zou, K. Ma, and K. S. Yeo, "A low phase noise and wide tuning range millimeter-wave VCO using switchable coupled VCO-cores," *IEEE Trans. Circuits Syst. I, Reg. Papers*, vol. 62, no. 2, pp. 554–563, Feb. 2015.

[11] Y. Chao and H. Luong, "Analysis and design of wide-band millimeter-wave transformer-based VCO and ILFDs," *IEEE Trans. Circuits Syst. I, Reg. Papers*, vol. 63, no. 9, pp. 1416–1425, Sep. 2016.

[12] A. Mazzanti and A. Bevilacqua, "On the phase noise performance of transformer-based CMOS differential-pair harmonic oscillators," *IEEE Trans. Circuits Syst. I, Reg. Papers*, vol. 62, no. 9, pp. 2334–2341, Sep. 2015.

[13] B. Sadhu, M. Ferriss, and A. Valdes-Garcia, "A 52 GHz frequency synthesizer featuring a 2nd harmonic extraction technique that preserves VCO performance," *IEEE J. Solid-State Circuits*, vol. 50, no. 5, pp. 1214–1223, May 2015.

[14] Z. Zong, M. Babaie, and R. B. Staszewski, "A 60 GHz frequency generator based on a 20 GHz oscillator and an implicit multiplier," *IEEE J. Solid-State Circuits*, vol. 51, no. 5, pp. 1261–1273, May 2016.

[15] A. H. M. Shirazi *et al.*, "On the design of mm-Wave self-mixing-VCO architecture for high tuning-range and low phase noise," *IEEE J. Solid-State Circuits*, vol. 51, no. 5, pp. 1210–1222, May 2016.

[16] P. Andreani, X. Wang, L. Vandi, and A. Fard, "A study of phase noise in colpitts and LC-tank CMOS oscillators," *IEEE J. Solid-State Circuits*, vol. 40, no. 5, pp. 1107–1118, May 2005.

[17] Z. Deng and A. M. Niknejad, "A 4-port-inductor-based VCO coupling method for phase noise reduction," *IEEE J. Solid-State Circuits*, vol. 46, no. 8, pp. 1772–1781, Aug. 2011.

[18] S. A.-R. Ahmadi-Mehr, M. Tohidian, and R. B. Staszewski, "Analysis and design of a multi-core oscillator for ultra-low phase noise," *IEEE Trans. Circuits Syst. I, Reg. Papers*, vol. 63, no. 4, pp. 529–539, Apr. 2016.

[19] L. Iotti, A. Mazzanti, and F. Svelto, "Insights into phase-noise scaling in switch-coupled multi-core LC VCOs for E-band adaptive modulation links," *IEEE J. Solid-State Circuits*, vol. 52, no. 7, pp. 1703–1718, Jul. 2017.

[20] G. Li and E. Afshari, "A distributed dual-band LC oscillator based on mode switching," *IEEE Trans. Microw. Theory Techn.*, vol. 59, no. 1, pp. 99–107, Jan. 2011.

[21] M. Taghivand, K. Aggarwal, and A. S. Y. Poon, "A 3.24-to-8.45 GHz low-phase-noise mode-switching oscillator," in *IEEE Int. Solid-State Circuits Conf. (ISSCC) Dig. Tech. Papers*, Feb. 2014, pp. 368–369.

[22] P. Andreani, K. Kozmin, P. Sandrup, M. Nilsson, and T. Mattsson, "A TX VCO for WCDMA/EDGE in 90 nm RF CMOS," *IEEE J. Solid-State Circuits*, vol. 46, no. 7, pp. 1618–1626, Jul. 2011.

[23] L. Fanori, A. Liscidini, and P. Andreani, "A 6.7-to-9.2 GHz 55 nm CMOS hybrid Class-B/Class-C cellular TX VCO," in *IEEE Int. Solid-State Circuits Conf. (ISSCC) Dig. Tech. Papers*, Feb. 2012, pp. 354–356.

[24] A. Goel and H. Hashemi, "Frequency switching in dual-resonance oscillators," *IEEE J. Solid-State Circuits*, vol. 42, no. 3, pp. 571–582, Mar. 2007.

[25] A. Mirzaei and A. A. Abidi, "The spectrum of a noisy free-running oscillator explained by random frequency pulling," *IEEE Trans. Circuits Syst. I, Reg. Papers*, vol. 57, no. 3, pp. 642–653, Mar. 2010.

[26] M. Babaie and R. B. Staszewski, "A study of RF oscillator reliability in nanoscale CMOS," in *Proc. 21st IEEE Eur. Conf. Circuit Theory Design*, Sep. 2013, pp. 243–246.

[27] M. Babaie and R. B. Staszewski, "An ultra-low phase noise class-F_2 CMOS oscillator with 191 dBc/Hz FoM and long-term reliability," *IEEE J. Solid-State Circuits*, vol. 50, no. 3, pp. 679–692, Mar. 2015.

Yatao Peng received the B.Eng. degree in information engineering from Tianjin Normal University, Tianjin, China, in 2010, and the Ph.D. degree in electronics engineering from the University of Chinese Academy of Sciences, Beijing, China, with a focus on the multi-band/wideband RF front-ended circuits in wireless communication station.

From 2016 to 2017, he was a Post-Doctoral Researcher with the University of Macau, Macau, China, where he was involved in CMOS millimeter-wave integretaed circuit design. From 2017 to 2018, he was with the National University of Singapore, Singapore, where he served as a Researcher to develop CMOS phase-shifter modules for hybrid integrated flexible electronic systems. He is currently a Scientist with the Advanced Quantum Architecture Laboratory, École Polytechnique Fédérale de Lausanne, Lausanne, Switzerland. His current research interests include CMOS cryogenic RF circuits for quantum compute application.

Jun Yin (M'14) received the B.Sc. and M.Sc. degrees in microelectronics from Peking University, Beijing, China, in 2004 and 2007, respectively, and the Ph.D. degree in electronic and computer engineering from the Hong Kong University of Science and Technology, Hong Kong, in 2013.

He is currently an Assistant Professor with the State Key Laboratory of Analog and Mixed-Signal VLSI, University of Macau, Macau, China. His current research interests include the CMOS RF integrated circuits for wireless communication and radar systems.

Pui-In Mak (S'00–M'08–SM'11) received the Ph.D. degree from the University of Macau (UM), Macau, China, in 2006.

He is currently a Full Professor with the Department of Electronic and Computer Engineering, Faculty of Science and Technology, UM, where he is also an Associate Director (Research) with the State Key Laboratory of Analog and Mixed-Signal VLSI. His current research interests include analog and radio-frequency circuits and systems for wireless and multi-disciplinary innovations.

Dr. Mak was the TPC Vice Co-Chair of ASP-DAC in 2016. He was a TPC Member of A-SSCC from 2013 to 2016, the ESSCIRC from 2016 to 2017, ISSCC since 2016. He was a member of Board-of-Governors of the IEEE Circuits and Systems Society from 2009 to 2011. He has been the Chair of the Distinguished Lecturer Program of IEEE Circuits and Systems Society since 2018. He was a co-recipient of the DAC/ISSCC Student Paper Award in 2005, the CASS Outstanding Young Author Award in 2010, the National Scientific and Technological Progress Award in 2011, the Best Associate Editor of the IEEE TRANSACTIONS ON CIRCUITS AND SYSTEMS II from 2012 to 2013, the A-SSCC Distinguished Design Award in 2015, the ISSCC Silkroad Award in 2016, and the Honorary Title of Value for Scientific Merits by the Macau Government in 2005. He was a Distinguished Lecturer of the IEEE Circuits and Systems Society from 2014 to 2015 and the IEEE Solid-State Circuits Society from 2017 to 2018. He has been inducted as an Overseas Expert of the Chinese Academy of Sciences since 2018. He was an Editorial Board Member of the IEEE Press from 2014 to 2016. He was the Senior Editor of the IEEE JOURNAL ON EMERGING AND SELECTED TOPICS IN CIRCUITS AND SYSTEMS from 2014 to 2015, an Associate Editor of the IEEE JOURNAL OF SOLID-STATE CIRCUITS since 2018, IEEE SOLID-STATE CIRCUITS LETTERS since 2017, and the IEEE TRANSACTIONS ON CIRCUITS AND SYSTEMS I from 2010 to 2011 and from 2014 to 2015, and the IEEE TRANSACTIONS ON CIRCUITS AND SYSTEMS II from 2010 to 2013.

Rui P. Martins (M'88–SM'99–F'08) was born in 1957. He received the bachelor's, master's, Ph.D., and Habilitation degrees for Full Professor in electrical engineering and computers from the Department of Electrical and Computer Engineering, Instituto Superior Técnico (IST), University of Lisbon, Lisbon, Portugal, in 1980, 1985, 1992, and 2001, respectively.

Since 1980, he has been with the Department of Electrical and Computer Engineering, IST, University of Lisbon, where he has been on leave since 1992. He is currently with the Department of Electrical and Computer Engineering, Faculty of Science and Technology (FST), University of Macau (UM), Macau, China, where he has been a Chair Professor since 2013. From 1994 to 1997, he was the Dean of the Faculty of the FST. Since 1997, he has been a Vice-Rector with UM. From 2001 to 2002, he was a Co-Founder of Chipidea Microelectronics (Macao) [now Synopsys] and in 2003, created the Analog and Mixed-Signal VLSI Research Laboratory, UM, elevated in 2011 to the State Key Laboratory of China (the first in Engineering in Macau), where he became a Founding Director. From 2008, after the reform of the UM Charter, he was nominated after open international recruitment, and reappointed in 2013 as a Vice-Rector (Research) until August 31, 2018. Within the scope of his teaching and research activities, he has taught 21 bachelor and master courses and, in UM, he has supervised (or co-supervised) 45 theses: Ph.D. (24) and Masters (21). He has co-authored 7 books and 11 book chapters, 442 papers, in scientific journals (141) and in conference proceedings (301), and other 64 academic works, in a total of 554 publications. He holds 28 U.S. patents and 2 Taiwan patents.

Dr. Martins was a Nominations Committee Member of the IEEE Circuits and Systems Society (CASS) in 2016 and 2017 and a member of the IEEE CASS Fellow Evaluation Committee in 2013, 2014, and 2019. He was a Founding Chairman of both the IEEE Macau Section from 2003 to 2005 and the IEEE Macau Joint-Chapter on CAS/Communications from 2005 to 2008 (2009 World Chapter of the Year of the IEEE CASS). He was the General Chair of the 2008 IEEE Asia–Pacific Conference on CAS in 2008 and a Vice President of Region 10 (Asia, Australia, and the Pacific) of the IEEE CASS from 2009 to 2011. He was a Vice President (World) of the Regional Activities and Membership of the IEEE CASS from 2012 to 2013. He was the CAS Society Representative in the Nominating Committee, for the election in 2014, of Division I (CASS/EDS/SSCS)—the Director of the IEEE. He was the General Chair of the ACM/IEEE Asia South Pacific Design Automation Conference—ASP-DAC'2016. He was the Chair of the IEEE CASS Fellow Evaluation Committee (Class 2018). In the representation of UM, he was one of the Vice Presidents from 2005 to 2014 and the President from 2014 to 2017 of the Association of Portuguese Speaking Universities. In July 2010, he was elected, unanimously, as a Corresponding Member of the Portuguese Academy of Sciences in Lisbon, and he is the only Portuguese Academician living in Asia. He was a recipient of the Medal of Professional Merit from Macao Government (Portuguese Administration) in 1999, the Honorary Title of Value from Macao SAR Government (Chinese Administration) in 2001, the IEEE Council on Electronic Design Automation Outstanding Service Award in 2016, and nominated the Best Associate Editor of TRANSACTIONS ON CAS II from 2012 to 2013. He served as an Associate Editor for the IEEE TCAS II: EXPRESS BRIEFS from 2010 to 2013.